Huang et al. *Zool. Res.* 2025, 46(3): 709−721
https://doi.org/10.24272/j.issn.2095-8137.2024.373
https://cstr.cn/32248.14.zr.2024.373

ZR | Zoological Research

Article Open Access

Features and mechanisms of long-lived *Myotis* somatic fibroblasts in response to DNA replication stress

Xiao-Yan Huang[1,2,3,5,#], Xiu-Yun Liu[1,2,3,5,#], Wei Wang[1,2,3,4,#], Gao-Jing Liu[1,2,3,5], You-Long Zhu[6], Xiao Wen[1,2,3,4], Kai-Qin Li[1,2,3,*], Bo Zhao[1,2,3,4,5,7,*]

[1] *Kunming Institute of Zoology*, *Chinese Academy of Sciences*, *Kunming*, *Yunnan* 650201, *China*

[2] *Key Laboratory of Genetic Evolution* & *Animal Models*, *Kunming Institute of Zoology*, *Chinese Academy of Sciences*, *Kunming*, *Yunnan* 650201, *China*

[3] *Key laboratory of Animal Models and Human Disease Mechanisms*, *Chinese Academy of Sciences*, *Kunming*, *Yunnan* 650201, *China*

[4] *Key Laboratory of Animal Models and Human Disease Mechanisms of the Chinese Academy of Sciences* & *Yunnan Province*, *and KIZ-CUHK Joint Laboratory of Bioresources and Molecular Research in Common Diseases*, *Kunming*, *Yunnan* 650201, *China*

[5] *University of Chinese Academy of Sciences*, *Beijing* 100049, *China*

[6] *Department of Hepatobiliary and Pancreatic Surgery*, *Second Affiliated Hospital of Kunming Medical University*, *Kunming*, *Yunnan* 650033, *China*

[7] *Primate Facility*, *National Research Facility for Phenotypic* & *Genetic Analysis of Model Animals*, *and National Resource Center for Non-Human Primates*, *Kunming Institute of Zoology*, *Chinese Academy of Sciences*, *Kunming*, *Yunnan* 650201, *China*

ABSTRACT

The DNA replication stress (RS) response is crucial for maintaining cellular homeostasis and promoting physiological longevity. However, the mechanisms by which long-lived species, such as bats, regulate RS to maintain genomic stability remain unclear. Also, recent studies have uncovered noncanonical roles of ribosome-associated factors in maintaining genomic stability. In this study, somatic skin fibroblasts from the long-lived big-footed bat (*Myotis pilosus*) were examined, with results showing that bat cells exhibited enhanced RS tolerance compared to mouse cells. Comparative transcriptome analysis under RS conditions revealed pronounced species-specific transcriptional differences, including robust up-regulation of ribosome biogenesis genes in bat cells and a markedly reduced activation of the P53 signaling pathway. These features emphasize a distinct homeostatic strategy in bat cells. Nuclear fragile X mental retardation-interacting protein 1 (*Nufip1*), a ribosome-associated factor highly expressed in bat fibroblasts, was identified as a potential integrator of ribosomal and P53 signaling via its association with ribosomal protein S27-like (Rps27l). These findings provide direct cellular and molecular evidence for a noncanonical RS response in bats, highlighting a deeper understanding of the biological characteristics and genomic maintenance mechanisms of long-lived species.

Keywords: Long-lived species; *Myotis pilosus*; DNA replication stress; Ribosome biogenesis; P53 signaling; Nufip1; Rps27l

INTRODUCTION

DNA replication stress arises when the progression of replication forks is impeded, resulting in delayed or stalled DNA synthesis and constituting a primary driver of genomic instability (Gaillard et al., 2015). To cope with this stress, cells initiate a coordinated DNA damage response that halts cell cycle progression, allowing time for repair. However, when damage surpasses repair capacity, cells undergo terminal fates such as senescence or apoptosis (Kitao et al., 2018). Senescence, a state in which somatic cells stop growing after repeated passaging or oncogenic stimuli (Nishimura et al., 2015), contributes to organismal aging and is implicated in many age-associated diseases. Clinical analyses of human skin biopsies have demonstrated an age-dependent accumulation of senescent cells, and epidemiological data have revealed strong correlations between senescence burden and the incidence of diseases such as osteoporosis, osteoarthritis, hypertension, and cerebral infarction (Heckenbach et al., 2022). Despite increasing evidence

Received: 20 March 2025; Accepted: 24 April 2025; Online: 25 April 2025

Foundation items: This work was supported by the Applied Basic Research Programs of Science and Technology Commission Foundation of Yunnan Province (202401AT070186 to K.Q.L., 202201AS070044 to B.Z.), Yunnan Province (202305AH340006 to B.Z.), and Kunming Science and Technology Bureau (2022SCP007 to B.Z.)

[#]Authors contributed equally to this work

*Corresponding authors, E-mail: kaiqinli@163.com; zhaobo@mail.kiz.ac.cn

demonstrating the correlation between disease and aging, effective therapeutic strategies targeting age-related degeneration remain limited.

Protein synthesis drives cellular growth, a process that necessitates stable and efficient ribosome biogenesis within the nucleolus. This complex process involves the transcription, modification, and processing of ribosomal RNA (rRNA), the production of ribosomal proteins (RPs) and associated factors, and the coordinated assembly of ribonucleoprotein particles into mature ribosomes. Ribosome biogenesis is the primary function of the nucleolus and requires the coordinated utilization of vast resources to maintain fidelity (Deisenroth & Zhang, 2010). Emerging evidence suggests that beyond its canonical role, ribosome biogenesis contributes to functions related to DNA replication stress. Several RPs participate in the RP-MDM2-P53 stress response pathway, a signaling cascade that functions as an important regulator of intracellular homeostasis. Various mitotic and genotoxic stressors converge on this pathway, inducing P53-dependent protective stress responses that lead to cell cycle arrest, apoptosis, DNA repair, and replicative senescence (Levine et al., 2006). The RP-MDM2-P53 signaling pathway is associated with ribosome biogenesis and serves as a critical checkpoint for ribosomal protein homeostasis (Franklin et al., 2023). Disruptions in ribosome biogenesis can trigger nucleolar stress, thereby activating this surveillance mechanism (Deisenroth & Zhang, 2010). Nevertheless, how ribosome biogenesis and P53 pathways are orchestrated remains unclear, and the identity of factors mediating this crosstalk is largely undefined.

Many exceptionally long-lived species have emerged as key models in longevity research, including the naked mole-rat (*Heterocephalus glaber*) (Azpurua et al., 2013), bowhead whale (*Balaena mysticetus*) (Keane et al., 2015; Liu et al., 2023), centenarians (Wang et al., 2024a), and various bat species (Wang et al., 2024c). Among these, bats are particularly noteworthy for their extraordinary lifespan relative to body size (Healy et al., 2014). Certain species, such as the little brown bat, Brandt's bat, mouse-eared bat, and Indian flying fox, can live up to 30–40 years (Tacutu et al., 2018), far exceeding the lifespan expected for mammals of similar size. The sustained preservation of genomic stability is recognized as a foundational determinant of longevity and a core mechanism related to aging (Gorbunova et al., 2020, 2007). Bats exhibit a robust capacity to preserve genome integrity through lifelong activation of DNA repair and damage signaling networks (Huang et al., 2016, 2019; Zhao et al., 2024). Additionally, comparative genomic analyses indicate that bats exhibit preferential up-regulation of genes involved in the mitotic cell cycle and DNA repair, enabling efficient damage recognition and recovery, along with mechanisms that limit oxidative stress and promote cellular resilience (Huang et al., 2016). Furthermore, signatures of positive selection have been detected in bat DNA repair genes (Huang et al., 2019; Zhang et al., 2013), yet direct experimental evidence detailing how bats maintain genomic stability remains limited.

To elucidate the cellular basis of this enhanced genome maintenance, primary skin fibroblasts derived from the big-footed bat (*Myotis pilosus*) (Li et al., 2022) and from mice (C57/BL6) were compared under DNA replication stress conditions. Bat cells exhibited greater replication fork stability and reduced accumulation of single-stranded DNA (ssDNA) damage, supporting sustained proliferation and low senescence under replication stress. Transcriptome profiling under stress conditions revealed significant interspecies differences in gene expression in response to replication stress, particularly in the P53 and ribosomal biogenesis pathways. Furthermore, we identified ribosome factors Nufip1 and Rps27l in crosslinking P53 and ribosomal biogenesis pathways. These findings provide novel mechanistic insight into how bats preserve genomic stability through coordinated modulation of translational and stress surveillance pathways, advancing the molecular understanding of longevity in mammals.

MATERIALS AND METHODS

Cells and culture conditions

Primary skin fibroblasts from big-footed bats and C57/BL6 mice were kindly provided by the Peng Shi Lab at the Kunming Institute of Zoology, Chinese Academy of Sciences (CAS). The A549 cell line was purchased from the Conservation Genetics CAS Kunming Cell Bank (China). All cells were cultured in Dulbecco's Modified Eagle's Medium (DMEM) (Gibco, Cat. no. C11995500BT, USA) containing 20% fetal bovine serum (FBS) (Alphabio, Cat. no. SA-201-1A, Australia), 100 U/mL penicillin, and 100 μg/mL streptomycin (Gibco, Cat. no. 15140-122, USA) under 37°C and 5% CO_2 conditions. All cells were expanded through 0.05% Trypsin/EDTA digestion (Gibco, Cat. no. 25200072, USA). All cells were authenticated at the Conservation Genetics CAS Kunming Cell Bank using short tandem repeat DNA profiling. Regular mycoplasma testing was performed using LookOut Mycoplasma polymerase chain reaction (PCR) detection (Sigma, Cat. No. MP0035, USA).

Reagents and antibodies

TRIzol reagent was purchased from Tiangen (Cat. no. DP424, China). DAPI-Fluoromount-G was purchased from Southern Biotech (Cat. no. C1320-P950, USA). 5-Chloro-2'-deoxyuridine (CldU) was purchased from Sigma (Cat. no. C6891-100mg, USA). 5-Iodo-2'-deoxyuridine (IdU) was purchased from Sigma (Cat. no. I7125-5G, USA). Hydroxyurea (HU) was purchased from Sigma (Cat. no. H8627-5G, USA). Gemcitabine (GEM) was purchased from Selleck (Cat. no. LY-188011, USA). SYBR™ Green was purchased from Life Technologies (Cat. no. A25778, USA). rProtein A/G Agarose Resin was purchased from Yeasen (Cat. no. 36404ES08, China). Normal melting agarose was purchased from Tsingke Biotech (Cat. no. TSJ001, China). Glycine was purchased from Sangon Biotech (Cat. no. A100167, China). Ribozinoindole-1 (Rbin-1) was purchased from MCE (Cat. no. HY-100816, USA). Pifithrin-α hydrobromide (PFT-α) was purchased from MCE (Cat. no. HY-15484, USA).

The following antibodies were obtained from the indicated suppliers: rat anti- 5-bromo-2'-deoxyuridine (BrdU) (Abcam, Cat. no. Ab6326, 1:1 000 for immunofluorescence, UK), mouse anti-BrdU (BD, Cat. no. 347580, 1:500 for immunofluorescence, USA), rabbit anti-Nufip1 (Proteintech, Cat. no. 12515-1-AP, 1:1 000 for immunofluorescence, 1:2 000 for immunoblotting, USA), rabbit anti-Rps27l (Proteintech, Cat. no. 15871-1-AP, 1:500 for immunofluorescence, 1:1 000 for immunoblotting, USA), mouse anti-Gapdh (Proteintech, Cat. no. 60004-1-lg, 1:5 000 for immunoblotting, USA), and mouse

anti-β actin (Proteintech, Cat. no. 66009-1-lg, 1:5000 for immunoblotting, USA). Secondary antibodies used for immunofluorescence were raised against rat (conjugated with Cyanine3, Thermo Fisher, Cat. no. A-10522, USA; conjugated with Alexa 488, Thermo Fisher, Cat. no. A-11006, USA), rabbit (conjugated with Cyanine3, Thermo Fisher, Cat. no. A-10520, USA), or mouse (conjugated with Alexa 488, Thermo Fisher, Cat. no. A11029, USA). Secondary antibodies used for immunoblotting were raised against rabbit (conjugated with horseradish peroxidase (HRP), Thermo Fisher, Cat. no. 31460, USA) or mouse (conjugated with HRP, Thermo Fisher, Cat. no. 31430, USA).

Cell proliferation assay

Cell proliferation was assessed using an Enhanced Cell Counting Kit-8 (CCK-8) (Beyotime, Cat. no. C0043, China) following the manufacturer's instructions. Cells were seeded into 96-well plates at a density of 3 000–5 000 cells per well. For each well, 10 μL of CCK-8 Reagent was added into 100 μL of culture medium. Plates were gently agitated and incubated at 37°C in a humidified atmosphere with 5% CO_2 for 0.5 to 4 h. Absorbance at 450 nm was measured using a microplate reader (Tecan, Switzerland). Absorbance values were proportional to the number of viable cells.

Senescence-associated β-galactosidase (SA-β-gal) staining

SA-β-gal staining was performed using a SA-β-gal staining kit (Beyotime, Cat. no. C0602, China) in accordance with the manufacturer's protocols. Cultured cells were first fixed with β-galactosidase staining fixative for 15 min, followed by three washes with phosphate-buffered saline (PBS). Cells were then incubated with staining solution overnight at 37°C, washed three times with PBS, and examined using an Inverted microscope (ECLIPSE Ti, Japan).

Immunoblotting

Cells were lysed in RIPA buffer (Beyotime Cat. no. P0013B, China). Protein concentrations were determined using protein assay dye (Bio-Rad, Cat. No. #5000006, USA) and NanoDrop spectrophotometric analysis (Maestrogen, China). Equal amounts of total protein were resolved using sodium dodecyl sulfate-polyacrylamide gel electrophoresis (SDS-PAGE) and transferred to polyvinylidene difluoride (PVDF) membranes (Merck Millipore, USA) at 300 mA for 2 h and 10 min at 4°C. Membranes were blocked with 5% skim milk in Tris-buffered saline (TBS) (W/V) containing 0.1% Tween 20 (TBS-T) for 1 h at room temperature. Primary antibody incubation was carried out overnight at 4°C in western blot primary antibody diluent (Beyotime, Cat. no. P0256, China). After three 10 min washes in TBS-T, membranes were incubated with HRP-conjugated secondary antibodies for 1 h at room temperature. Following another three washes in TBS-T at room temperature, protein bands were visualized using a chemiluminescence image analysis system (Tanon 5200, China) after incubation with SuperSignal West Pico PLUS Chemiluminescent Substrate (Thermo Fisher, Cat. No. 34580, USA).

Quantitative reverse transcription PCR (RT-qPCR)

Total RNA was isolated using TRIzol reagent according to the manufacturer's instructions. Extracted RNAs were used for reverse-transcriptase PCR (RT-PCR) with a Reverse Transcription kit (Takara, cat. no. RR047A, Japan). Quantitative PCR (qPCR) was performed using PowerUp SYBR Green Master Mix (Invitrogen, Cat. no. A25742, USA) on the Bio-Rad Real-Time PCR platform (Bio-Rad, CFX Connect™, USA). Primer sequences used for RT-qPCR are provided in Supplementary Table S1.

Immunofluorescence

Immunofluorescence assays, including co-localization of Nufip1 with replication forks, were conducted as described previously (Tu et al., 2022), with modifications for ssDNA damage. Cells were pulse-labeled with 25 μmol/L CldU for 48 h, fixed in 4% paraformaldehyde (PFA) (Sangon, Cat. no. C10488-500g, China), permeabilized with 0.2% Triton X-100 (Diamond, Cat. No. A110694-010, China) for 20 min, and blocked with 1% Bovine Serum Albumin (BSA, MP Biomedicals, Cat. no. FC0077, USA) for 1 h at room temperature. Cells were then incubated overnight at 4°C with rat anti-BrdU primary antibody and labeled with fluorescent secondary antibodies for 1 h at room temperature. Nuclei were stained using DAPI and images were captured using a confocal microscope (Olympus, FV1000, Japan).

DNA fiber assay

Replication dynamics were assessed using DNA fiber labeling. Cells were sequentially incubated with 50 μmol/L IdU for 20 min, with or without HU or GEM treatment, followed by 50 μmol/L CldU for second labeling. Approximately 4 500 labeled cells were resuspended in 2.5 μL of suspension and dropped onto one end of a glass slide (CITOTEST, Cat. no. 10127105P-G, China), followed by 12 μL of lysis buffer (50 mmol/L EDTA, 0.5% SDS, and 200 mmol/L tris-HCl (pH 7.5)) and incubation for 1 min at room temperature. Subsequently, the slides were tilted to 15° to spread the DNA fibers along the slide, followed by treatment with 2.5 mol/L HCl and incubation with rat anti-BrdU (BU1/75) and mouse anti-BrdU monoclonal antibodies. Secondary antibodies included Alexa Fluor Cy3-conjugated goat anti-rat and Alexa Fluor 488-conjugated goat anti-mouse, respectively. Images were captured using a confocal microscope (Olympus, FV1000, Japan). ImageJ software v.1.8.0 was used to measure DNA fiber length, with conversion to kilobase pairs using 1 μm=2.59 kb.

Constructs and lentiviral infection

Short hairpin RNA (shRNA) sequences are provided in Supplementary Table S2. The shRNAs were cloned into pLKO.1 vectors using enzymatic sites Age I/EcoR I. For lentiviral production, pLKO.1-shRNA or pLVX expression plasmids were co-transfected into HEK293T cells with packaging plasmids pCMVΔ8.1 and pMD2.G at a ratio of 5:2.5:1 using PEI Transfection Reagent (Sigma-Aldrich, Cat. no. 408727-100ML, USA). Viral supernatants were harvested and filtered through a 0.45 μm filter (Millipore, Cat. no. SLHV033RB, USA) 48 h post transfection.

Co-immunoprecipitation (Co-IP)

Primary skin fibroblasts from big-footed bats and C57/BL6 mice were harvested and washed twice with ice-cold PBS, then lysed with 1× RIPA lysis buffer (Beyotime, P0013J, China) containing complete EDTA-free (Roche, 11836170001, USA) inhibitors. Lysates were treated with DNase I (10 U/mL; New England Biolabs, Cat. no. M0303, USA) to eliminate nucleic acid-mediated interactions. Co-immunoprecipitation was performed using anti-Nufip1 or anti-Rps27l antibodies, with normal IgG as negative control. Lysates were incubated with primary antibodies overnight at 4°C, followed by precipitation with Protein A/G agarose resin (Yeasen, Cat. no. 36404ES08, China) according to the manufacturer's protocols.

After sequential washing, immune complexes were resolved by SDS-PAGE and subjected to immunoblotting.

RNA sequencing and bioinformatic analysis

Total RNA was isolated from the bat and mouse fibroblasts using TRIzol reagent following the manufacturer's protocols. After validation of RNA quality and integrity, RNA libraries were constructed using a NEBNext Ultra RNA Library Prep Kit (Illumina, Cat. no. E7530S, USA). Libraries were sequenced on an Illumina PE150 platform to generate paired-end 150 bp reads. Clean data were obtained by removing adapter sequences, low-quality reads, and low-quality bases using Trimmomatic v.0.36 with default parameters. Transcript quantification was conducted using RSEM, and differential expression analysis of one-to-one orthologous protein-coding genes was performed using DESeq2 (|fold-change|>2, *P*-adjust<0.05). Differentially expressed genes (DEGs) were subjected to Kyoto Encyclopedia of Genes and Genomes (KEGG) and Gene Ontology (GO) enrichment analyses using KOBAS-i.

P53 activation reporter assay

The pp53-TA-luc reporter plasmid was kindly provided by the Yu-Han Zhao lab at the Kunming Institute of Botany, CAS. The plasmid was transfected into A549 cells using Lipofectamine 3000 (Thermo Fisher, Cat. no. L3000015, USA). At 48 h post-transfection, luminescence was measured using a Dual-Luciferase Reporter Assay System (Promega, Cat. no. E1960, USA) and Luminoskan Ascent instrument (Thermo Fisher, USA).

Statistical analysis and reproducibility

Experiments were repeated three times unless otherwise stated. All statistical analyses were conducted using GraphPad Prism v.9 (GraphPad, USA). Student's *t*-test was performed to determine *P*-values of the raw data unless otherwise stated, with $P<0.05$ considered significant. Representative images are shown unless otherwise stated. Quantitative data are expressed as mean±standard error of the mean (SEM) unless otherwise stated. Imaging analyses were conducted by investigators blinded to experimental conditions; analyses were not randomized but included parallel examination of all experimental groups.

RESULTS

***Myotis* fibroblasts exhibit enhanced resistance to chemically induced replication stress**

Genomic and transcriptomic studies have shown that long-lived *Myotis* bats exhibit marked enrichment of gene clusters involved in DNA replication, suggesting a potential enhancement in replication stress response mechanisms (Huang et al., 2016). However, direct experimental validation has remained lacking. In this study, replication dynamics in primary skin fibroblasts from the big-footed bat (MySF) were examined and compared with those from C57BL/6 mouse fibroblasts (MSF) using the DNA fiber assay, a single-molecule method for DNA replication kinetics and stability (Quinet et al., 2017). Replication stress was induced using HU or GEM (Ercilla et al., 2020; Jiang et al., 2023), and key parameters, including fork velocity, nascent DNA stability, fork restart efficiency, and fork recovery, were analyzed (Figure 1A). Under normal culture conditions, MySF exhibited a slightly reduced fork velocity relative to MSF (Figure 1B, C). Following treatment with 1 mmol/L HU, MSF displayed pronounced destabilization of nascent DNA, while MySF maintained fork integrity (Figure 1B, D). Comparable protection was observed under 10 μmol/L GEM treatment (Figure 1E). Fork restart efficiency (Figure 1F) and recovery (Figure 1G) under HU treatment revealed no significant differences between MySF and MSF, indicating that the primary distinction lies in the enhanced ability of MySF to preserve nascent strand stability.

Given that impaired protection in nascent DNA may induce ssDNA breaks and contribute to genomic instability and cellular senescence (Caldecott, 2024; Wu et al., 2024), ssDNA breakage was quantified under HU and GEM conditions. Indeed, both treatments led to elevated ssDNA breaks in MSF, whereas MySF showed minimal damage accumulation (Figure 1H–J), consistent with the DNA fiber assay results. Regarding cell fate determination, the CCK-8 assay was conducted to evaluate cellular viability. Under untreated conditions, MySF and MSF displayed comparable proliferation rates. However, under 0.4 mmol/L HU (Supplementary Figure S1A) or 1 μmol/L GEM exposure (Supplementary Figure S1B), MSF growth was markedly inhibited, while MySF showed only a modest decline. After 24 h of HU treatment, MySF and MSF showed relative proliferation rates of approximately 80% and 50%, respectively. By 48 h, these declined to 70% in MySF and 30% in MSF, and at 72 h, to 50% and 27%. At 96 h, MySF stabilized near 50%, whereas MSF fell to 20% and continued declining. A similar pattern was observed under GEM treatment, indicating that MySF maintained superior viability under replication stress.

Morphological analysis revealed that HU- or GEM-treated MSF displayed enlarged, flattened phenotypes characteristic of stress-induced senescence (Sikora et al., 2021). To investigate this further, a long-term low-dose exposure protocol (1 μmol/L HU or 10 nmol/L GEM for 15 days) was implemented. Quantification of SA-β-gal-positive cells revealed that more than 60% of MSF became senescent after 15 days HU treatment, compared to only around 18% of MySF (Supplementary Figure S1C, D). Similar results were observed under GEM treatment (Supplementary Figure S1E, F). Collectively, these findings demonstrate that MySF possess superior intrinsic capacity to tolerate chemically induced replication stress compared to MSF.

Ribosome biogenesis is selectively enriched in MySF during replication stress

To determine the transcriptional mechanisms underlying the enhanced stress resilience observed in MySF, bulk RNA sequencing was performed on MySF and MSF following treatment with or without 1 mmol/L HU for 4 h (Figure 2A). Principal component analysis (PCA) confirmed the reliability of the transcriptomic data (Supplementary Figure S2A, B). Differential expression analysis identified distinct transcriptional responses to HU exposure between the two cell types. Genes exhibiting >2-fold change were quantified (Supplementary Figure S2C). Volcano plots of DEGs revealed that *Tgfbi*, *Mical2*, and *Lrrc32* ranked highest among the up-regulated genes in MySF (Supplementary Figure S2D), while *Sema7a*, *Btg2* and *Cdkn1a* ranked highest among the up-regulated genes in MSF (Supplementary Figure S2E). These genes are involved in oncogenesis (e.g., *Tgfbi* (Wang et al., 2024b), *Mical2* (Makiuchi et al., 2024), *Sema7a* (Ochman et al., 2024), and *Cdkn1a* (Alshamrani et al., 2024)), the

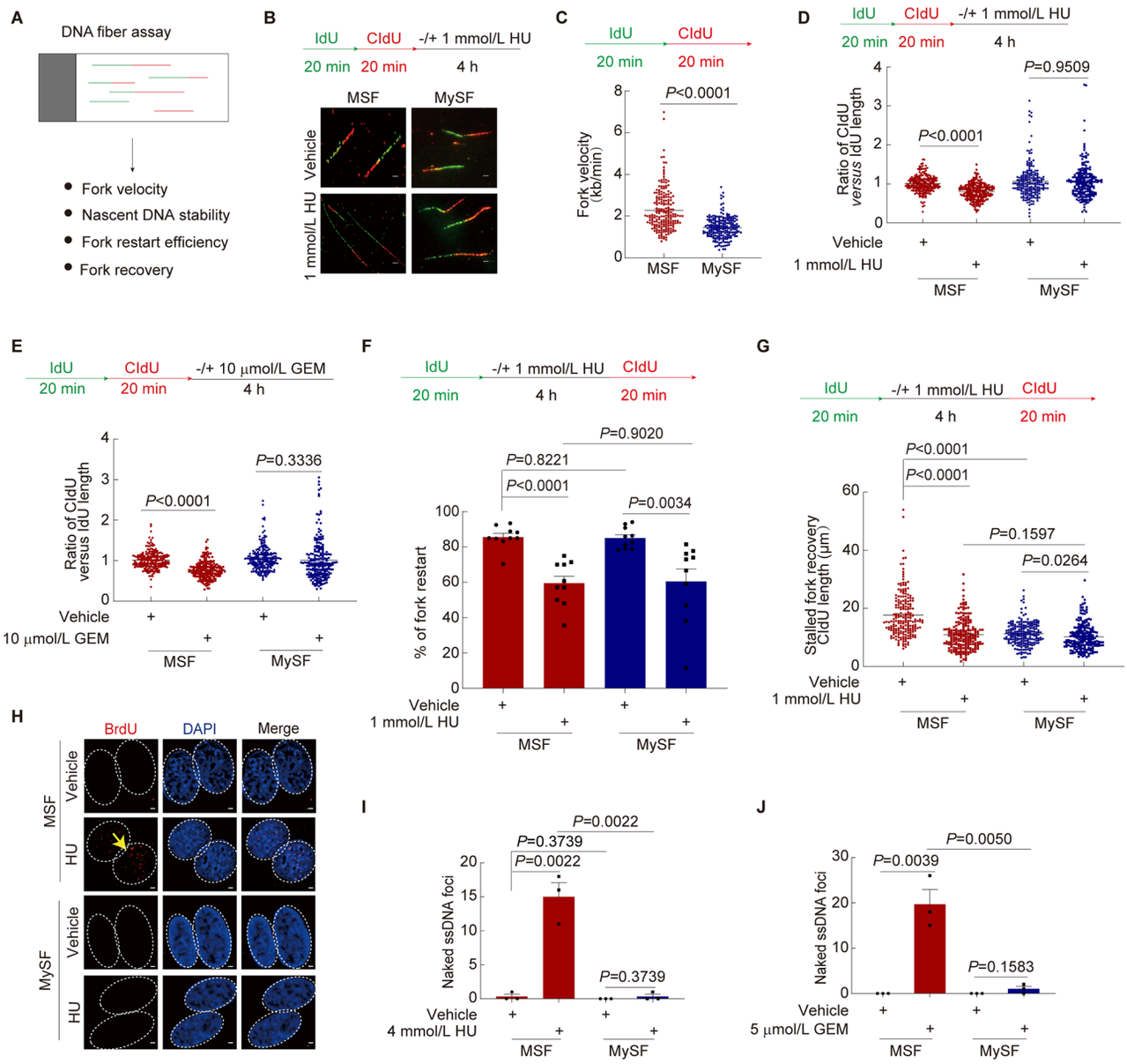

Figure 1 Myotis fibroblasts exhibit enhanced nascent DNA protection compared to mouse cells

A: Schematic of DNA fiber assay. B: Representative images of nascent DNA stability in MySF and MSF under 1 mmol/L HU treatment. Scale bar: 10 μm. C: Quantification of fork velocity. D, E: Quantification of nascent DNA stability in MySF and MSF under 1 mmol/L HU (D) and 10 μmol/L GEM (E) treatment, calculated as the ratio of CldU to IdU tract lengths. At least 200 single forks were calculated per sample. F, G: Quantification of fork restart rate (F) and stalled fork recovery length (G) in MySF and MSF following 1 mmol/L HU exposure. At least 200 single forks were calculated per sample. H–J: Representative images (H) and statistical results (I, J) of ssDNA generation induced by 4 mmol/L HU (H, I) and 5 μmol/L GEM (J) in MySF and MSF. ssDNA was labeled and detected under nondenaturing conditions. At least 200 cells from three independent experiments were analyzed. Scale bar: 10 μm.

nervous system (e.g., *Btg2* (Li et al., 2024)), and immune modulation (e.g., *Lrrc32* (Lubin et al., 2022)).

Given previous reports linking ribosomal activity and P53 signaling in stress-induced cellular senescence (Nishimura et al., 2015; Deisenroth & Zhang, 2010; Franklin et al., 2023), functional enrichment analysis of DEGs was conducted using KEGG and GO frameworks. Under replication stress, MySF displayed significant up-regulation of genes associated with ribosome biogenesis (Supplementary Figure S2F, G), alongside suppression of genes related to mitotic nuclear division and axon guidance (Supplementary Figure S2H, I). In contrast, MSF showed up-regulation in pathways related to cytokine-cytokine receptor interaction and muscle cell proliferation (Supplementary Figure S2J, K), and down-regulation in pathways involved in the cell cycle and mitotic nuclear division (Supplementary Figure S2L, M). These findings indicate that MySF cells respond to replication stress by preferentially activating genes related to ribosome biogenesis, whereas MSF cells exhibit a marked impairment in proliferation. Integrated pathway analysis further revealed that ribosome-associated pathways were up-regulated in MySF, while P53 signaling was more strongly induced in MSF (Figure 2B). To validate these observations, representative genes from both pathways were selected for analysis. Heatmap and qPCR data confirmed the elevation of ribosome pathway-related genes in MySF, as well as greater up-

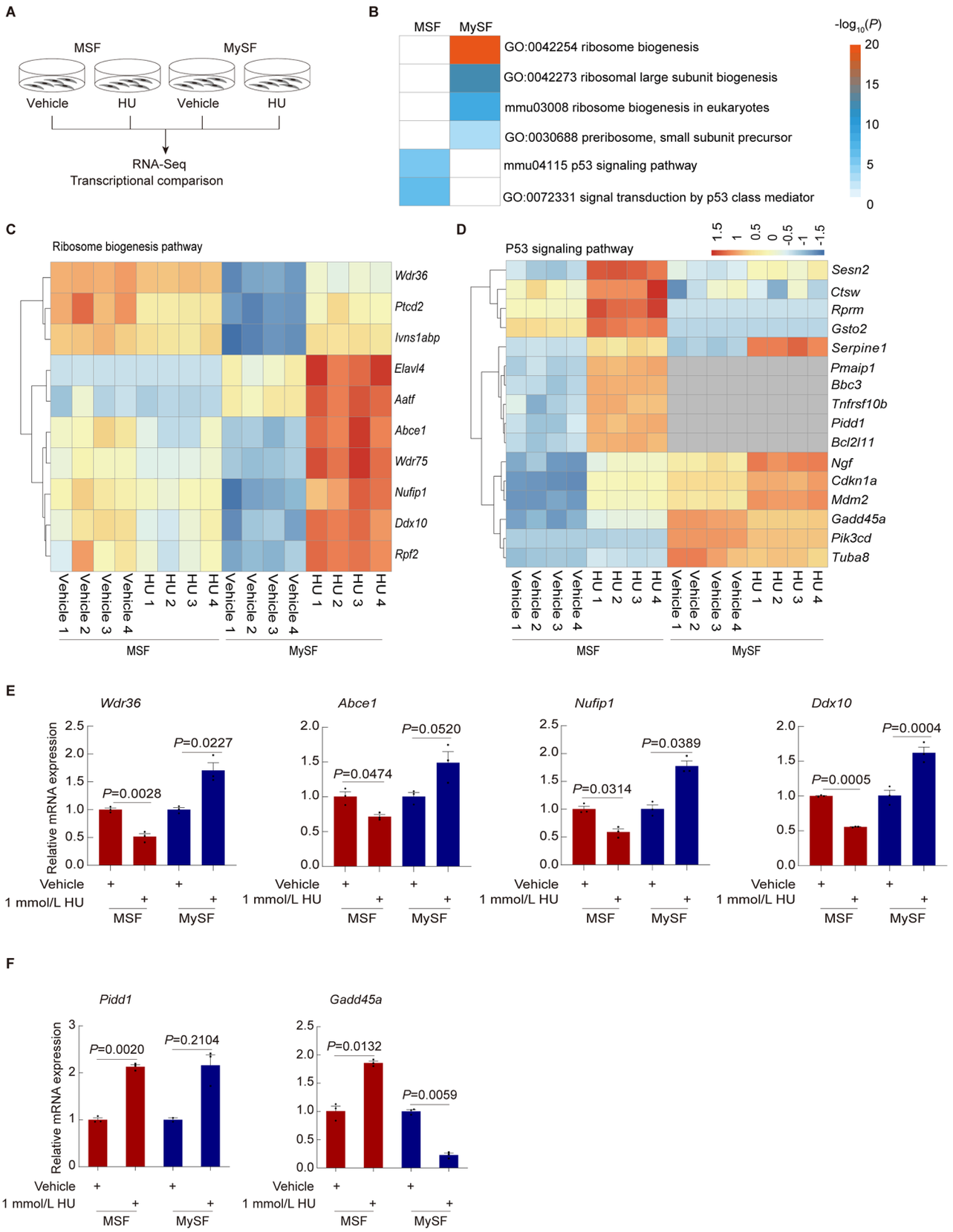

Figure 2 Enrichment of ribosome biogenesis pathway in MySF under replication stress

A: Schematic of sample collection and RNA-seq. B: Top enriched pathways based on GO and KEGG analyses of highly expressed genes in MySF versus MSF (FPKM fold-change>2), ranked by Rich factors. C, D: Heatmap showing differential expression of genes associated with the ribosome biogenesis pathway (C) and P53 signaling pathway (D) in MySF and MSF. E, F: RT-qPCR detection of ribosome biogenesis pathway (E) and P53 signaling pathway genes (F) in MySF and MSF with or without 1 mmol/L HU treatment. Data represent mean±SEM. *n*=3 biologically independent experiments. *P*-values were calculated using a two-tailed *t*-test.

regulation of P53 pathway-related genes in MSF in response to replication stress (Figure 2C–F).

Functional analysis of ribosomal gene *Nufip1* in MySF and MSF under replication stress

Transcriptome profiling revealed that *Nufip1*, a gene associated with ribosome function, was markedly up-regulated in MySF in response to chemically induced replication stress, while remaining minimally expressed in MSF. Given its known roles in rRNA processing (McKeegan et al., 2007), ribonucleoprotein (RNP) assembly, and ribophagy, *Nufip1* was identified as a candidate effector mediating replication stress resilience in bat cells. Both qPCR and immunoblotting confirmed significantly higher expression of *Nufip1* in MySF relative to MSF under both basal conditions and upon exposure to 1 mmol/L HU or 10 μmol/L GEM (Figure 3A, B; Supplementary Figure S2N).

To investigate the functional contribution of *Nufip1*, targeted knockdown was performed in MySF using three specific shRNAs (Figure 3C). Knockdown of *Nufip1* led to substantial accumulation of ssDNA breaks under HU or GEM treatment, reaching levels comparable to those observed in MSF (Figure 3D, E). In addition, knockdown of *Nufip1* significantly inhibited cell proliferation under both HU (Figure 3F) and GEM exposure (Figure 3G), and markedly increased SA-β-gal activity in treated MySF (Figure 3H, I). To determine whether this protective phenotype was dependent on passage number, early-passage (<10) and late-passage (>50) MySF were compared. Results showed that both early and advanced MySF cells displayed similar phenotypes in terms of nascent DNA protection under replication stress (Figure 3J, K). For further validation, the *Nufip1* coding sequence (CDS) was ectopically expressed in MSF to generate *Nufip1*-overexpressing cells (Figure 4A, B). Following puromycin selection, DNA fiber assays revealed that *Nufip1* overexpression enhanced nascent strand protection in MSF under replication stress (Figure 4C, D). To clarify the functional roles of ribosome biogenesis in fork stability, MSF cells were treated with the ribosome biogenesis inhibitor Rbin-1, followed by DNA fiber assays to determine nascent DNA stability under replication stress induced by HU (Figure 4C) or GEM (Figure 4D) exposure. Rbin-1 treatment abolished the protective effect of *Nufip1* on nascent DNA stability, confirming the functional link between *Nufip1* activity and ribosome-dependent fork stability. Consistently, overexpression of *Nufip1* reduced ssDNA damage and preserved cell proliferation under HU treatment (Figure 4E–G), supporting its role in replication stress response and cellular fitness. However, subcellular localization analysis via immunofluorescence showed that *Nufip1* was predominantly nuclear, with no significant co-localization with BrdU-labeled DNA replication foci (Figure 4H), suggesting an indirect mode of action in replication stress response. To assess whether sequence divergence in Nufip1 contributes to functional differences between species, a comparative analysis of the CDS (Supplementary Figure S3) and amino acid sequences (Supplementary Figure S4) was conducted for mouse and bat Nufip1. The bat Nufip1 protein featured a longer C-terminal, which may participate in replication stress adaptation, although its precise role remains unclear.

Proteomic interactome analysis reveals potential link between Nufip1 and Rps27l-Mdm2-P53 pathway

To determine the molecular mechanism by which Nufip1 contributes to replication stress tolerance, an immunoprecipitation-mass spectrometry strategy was employed. MySF and MSF samples, treated with or without 1 mmol/L HU or 10 μmol/L GEM for 4 h, were processed in parallel for analysis (Figure 5A). Isotype IgG was included as a non-specific binding control. The total number of specific Nufip1-associated proteins identified under each condition is summarized in Figure 5B. Functional enrichment analysis of Nufip1-interacting proteins was conducted (Huttlin et al., 2017). Under normal culture conditions, Nufip1-associated networks in MySF were enriched in glutathione metabolism, while MSF were enriched in proteasome-related pathways (Figure 5C, D). Upon HU exposure, MySF and MSF exhibited enrichment in the ribosome biogenesis and viral carcinogenesis pathways, respectively (Figure 5E, F). In response to GEM exposure, MySF and MSF were enriched in the coronavirus disease and ribosome pathways, respectively (Figure 5G, H). Notably, both the coronavirus disease and ribosome pathways were consistently enriched in MySF under HU and GEM treatment but were absent in MSF. These patterns suggest that drug-induced replication stress disrupts ribosomal homeostasis in MSF cells.

Among the identified interactors, Rps27l displayed stable interaction with Nufip1, which was slightly enhanced under HU and GEM treatment (Figure 6A, B). Co-immunoprecipitation in MySF confirmed the interaction between Nufip1 and Rps27l (Figure 6C, D), with Gapdh serving as a negative control. Rps27l is a known modulator of the Mdm2-P53 pathway, promoting P53 stabilization by antagonizing Mdm2 binding (Xiong et al., 2014). To assess whether Nufip1 influences this regulatory node, immunofluorescence staining experiments were performed to examine Nufip1 subcellular localization. Results showed that knockdown of *Nufip1* increased nuclear accumulation of Rps27l in MySF under replication stress (Figure 6E, F). To evaluate the functional consequence of Nufip1 modulation on P53 activity, a pp53-TA-luc reporter was delivered into A549 cells, with subsequent exposure to 10 μmol/L etoposide to activate the P53 pathway (Figure 6G, H). Results demonstrated that *NUFIP1* knockdown led to a pronounced increase in P53 activity (Figure 6I), suggesting strong inhibitory effects of NUFIP1 on P53. Conversely, pharmacological inhibition of P53 using PFT-α diminished nuclear enrichment of NUFIP1 in etoposide-treated A549 cells (Supplementary Figure S5A), suggesting mutual regulation of P53 and NUFIP1. Furthermore, RT-qPCR revealed that *Nufip1* knockdown reduced *Mdm2* expression in MySF cells (Figure 6J, K). Expression of the downstream effector *p21* was markedly lower in MySF compared to MSF (Figure 6L), consistent with the observed capacity of bat fibroblasts to maintain cell proliferation in genotoxic conditions. To determine the conservation of this function across cell types, NUFIP1 knockdown was performed in non-fibroblast human A549 cells. Results showed that *NUFIP1* knockdown in A549 cells also impaired nascent fork stability under both HU- and GEM-induced replication stress conditions (Supplementary Figure S5B, C). Collectively, these results suggest that Nufip1 may promote cell tolerance to replication stress by inhibiting P53 signaling, with P53 signaling a determinant of nuclear enrichment of NUFIP1.

DISCUSSION

Myotis bats represent a notable exception among mammals, exhibiting remarkable longevity relative to body size and

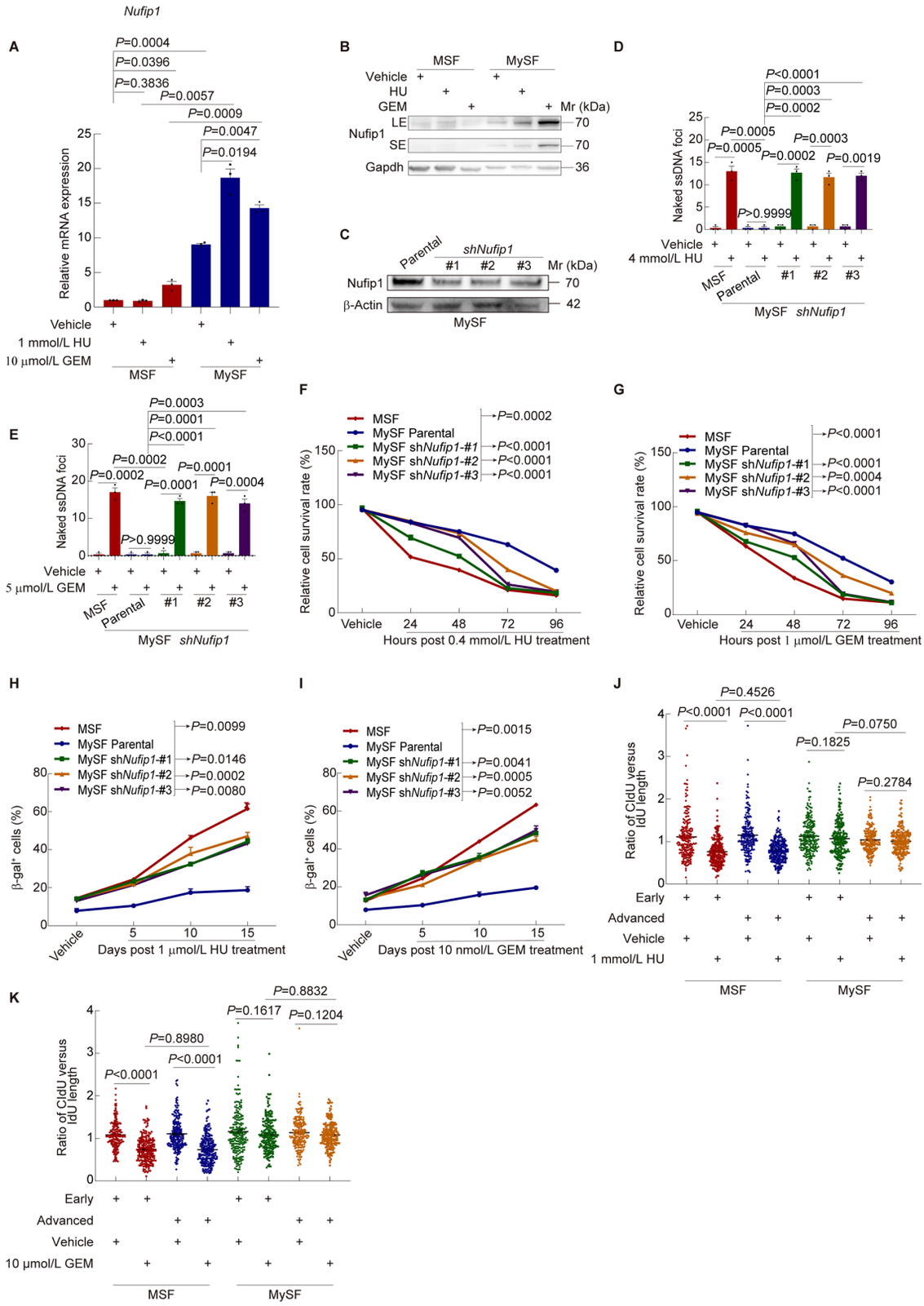

Figure 3 Functional analysis of ribosomal gene *Nufip1* in MySF under replication stress

A: RT-qPCR analysis of *Nufip1* expression in MySF and MSF with or without 1 mmol/L HU or 10 μmol/L GEM. B: Immunoblotting of Nufip1 protein levels in MySF and MSF with or without 1 mmol/L HU or 10 μmol/L GEM. Gapdh was used as a loading control. C: Immunoblotting of Nufip1 expression in MySF with or without knockdown. β-actin was used as a loading control. D, E: Quantification of ssDNA generation induced by 4 mmol/L HU (D) and 5 μmol/L GEM (E) in MySF with and without *Nufip1* knockdown and in MSF. F, G: Relative proliferation rates of MySF with or without *Nufip1* knockdown and of MSF cells under 0.4 mmol/L HU (F) and 1 μmol/L GEM (G) treatment at 0, 24, 48, 72, and 96 h, measured by CCK-8 assay. H, I: Quantification of SA-β-gal-positive MySF and MSF under 1 μmol/L HU (H) and 10 nmol/L GEM (I) treatment at 0, 5, 10, and 15 days. J, K: Quantification of nascent DNA stability in MySF and MSF between early (<10) and advanced passages (>50) under 1 mmol/L HU (J) and 10 μmol/L GEM (K) treatment, calculated as the ratio of CldU to IdU tract length. At least 200 single forks were calculated per sample.

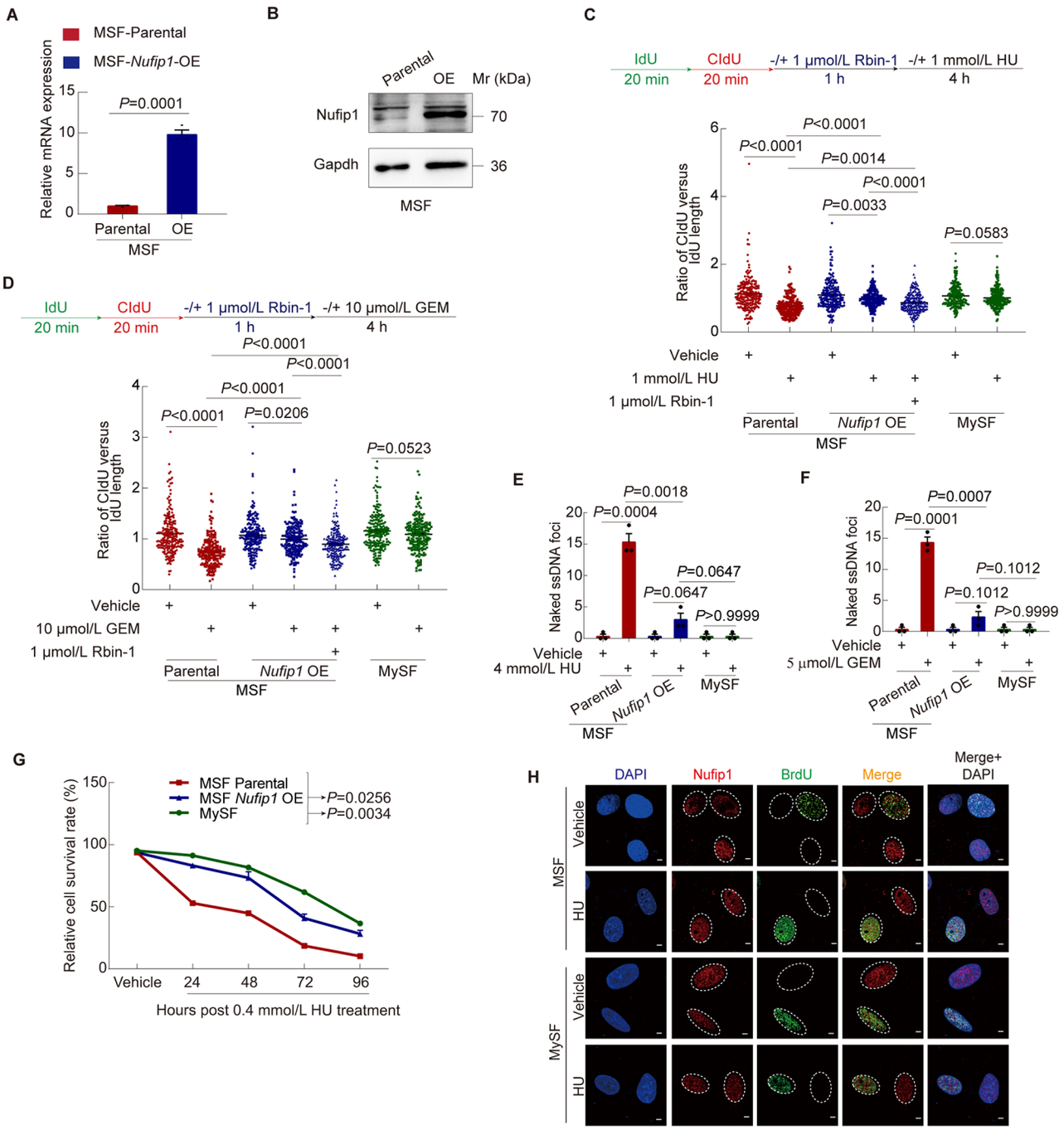

Figure 4 Nufip1 coordinates nascent DNA strand stability under replication stress and supports cell proliferative capacity

A, B: RT-qPCR (A) and immunoblot (B) analysis of *Nufip1* expression in MSF with or without *Nufip1* overexpression. C, D: Quantification of nascent DNA stability in MySF and MSF with or without *Nufip1* overexpression under 1 mmol/L HU (C) and 10 μmol/L GEM (D), as well as 1 μmol/L Rbin-1 treatment, calculated as the ratio of CldU to IdU tract length. At least 200 single forks were calculated per sample. E, F: Quantification of ssDNA generation induced by 4 mmol/L HU (E) and 5 μmol/L GEM (F) in MySF and MSF with or without *Nufip1* overexpression. G: Relative proliferation rates of MySF and MSF with or without *Nufip1* overexpression under 0.4 mmol/L HU treatment at 0, 24, 48, 72, and 96 h, measured by CCK-8 assay. H: Immunofluorescence detection of subcellular localization of Nufip1 and its co-localization with replication forks. Scale bar: 5 μm. Data represent mean±SEM. *n*=3 biologically independent experiments. *P*-values were calculated using a two-tailed *t*-test.

metabolic rate. While recent genomic and transcriptomic investigations have provided preliminary clues regarding their biological characteristics (Hua et al., 2024; Seim et al., 2013; Tyshkovskiy et al., 2023; Zhang et al., 2013), experimental evidence at the cellular level remains limited. Previous studies have highlighted the capacity of *Myotis* species to resist cellular senescence (Gorbunova et al., 2020; Wang et al., 2024c) and maintain genomic stability throughout their lifespan (Gorbunova et al., 2020; Huang et al., 2016, 2019). Nevertheless, current conclusions are largely based on speculative omics data and lack mechanistic validation. MySF demonstrated enhanced preservation of nascent DNA strands, reduced single-stranded DNA accumulation, and sustained proliferative capacity under replication stress. These phenotypes indicate that MySF possess intrinsic mechanisms that actively stabilize replication forks and maintain genome

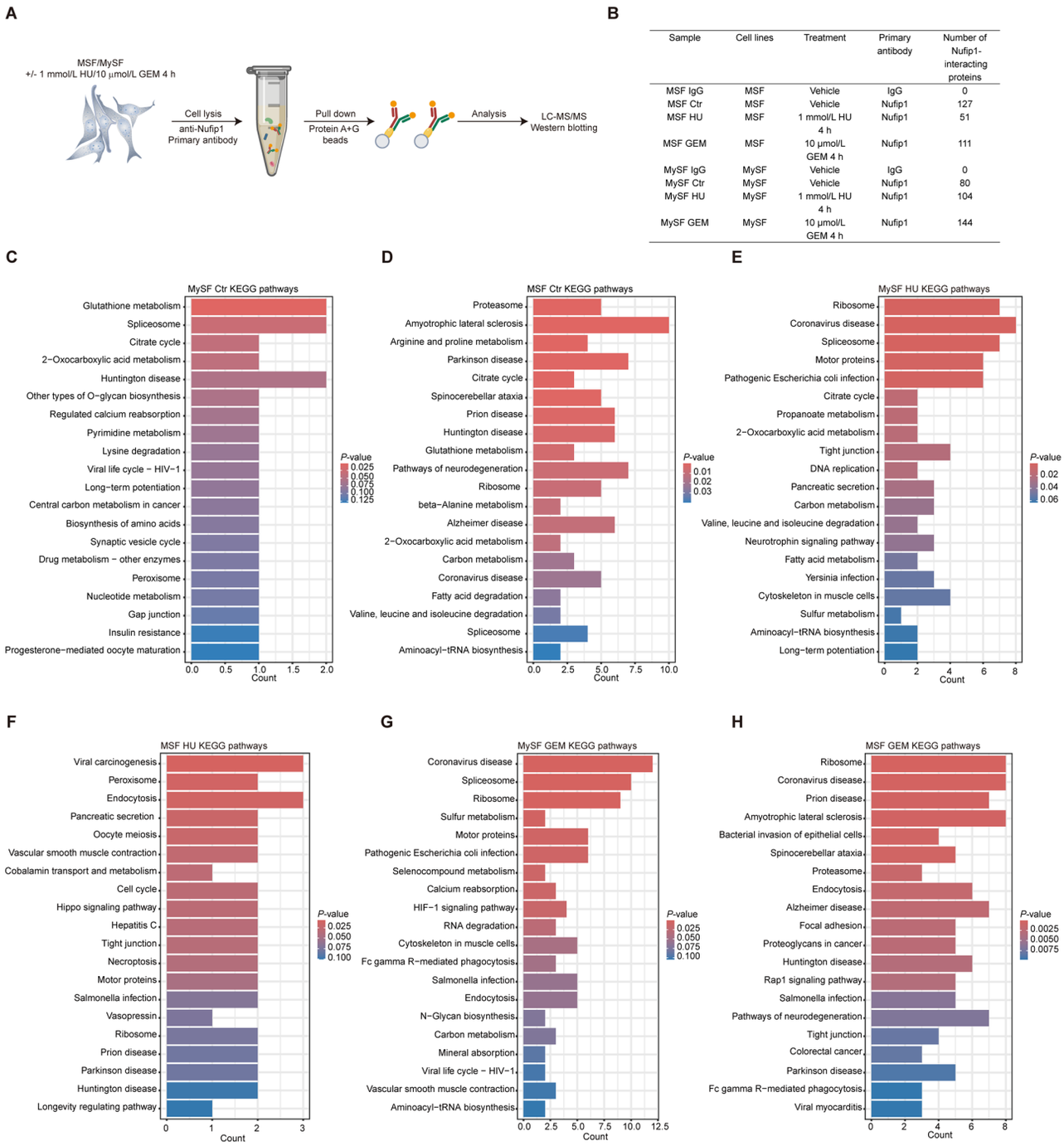

Sample	Cell lines	Treatment	Primary antibody	Number of Nufip1-interacting proteins
MSF IgG	MSF	Vehicle	IgG	0
MSF Ctr	MSF	Vehicle	Nufip1	127
MSF HU	MSF	1 mmol/L HU 4 h	Nufip1	51
MSF GEM	MSF	10 μmol/L GEM 4 h	Nufip1	111
MySF IgG	MySF	Vehicle	IgG	0
MySF Ctr	MySF	Vehicle	Nufip1	80
MySF HU	MySF	1 mmol/L HU 4 h	Nufip1	104
MySF GEM	MySF	10 μmol/L GEM 4 h	Nufip1	144

Figure 5 Endogenous Co-IP analysis of Nufip1-interacting proteins

A: Schematic of Co-IP and liquid chromatography-tandem mass spectrometry (LC-MS/MS) analysis of MySF and MSF with or without 1 mmol/L HU or 10 μmol/L GEM exposure, using anti-Nufip1 antibody. Isotype IgG served as a negative control. B: Summary table showing number of Nufip1-interacting proteins identified in each group. C, D: KEGG pathways analysis of Nufip1-interacting proteins under normal culture conditions in MySF (C) and MSF (D). E, F: KEGG pathways analysis of Nufip1-interacting proteins under 1 mmol/L HU treatment in MySF (E) and MSF (F). G, H: KEGG pathways analysis of Nufip1-interacting proteins under 10 μmol/L GEM treatment in MySF (G) and MSF (H).

integrity. Transcriptomic analysis further revealed significant differences in gene expression profiles in MySF and MSF under replicative stress, especially in the up-regulation of ribosomal biogenesis and P53 signaling. This divergence suggests that *Myotis* cells possess a unique homeostatic regulatory mechanism. Among the ribosome-related genes up-regulated in MySF, *Nufip1* emerged as a key effector. Functional assays —via knockdown in bat cells and overexpression in mouse cells —confirmed that *Nufip1* contributes to replication stress resilience and intracellular homeostasis in *Myotis*. Proteomic analysis through immunoprecipitation and mass spectrometry identified species-specific interaction protein profiles of Nufip1 and established Rps27l as a putative binding partner. In conclusion, these findings provide direct cellular and molecular evidence of the biological characteristics of *Myotis*.

Several aspects of the current study are worthy of further discussion. First, *Nufip1* was significantly up-regulated in

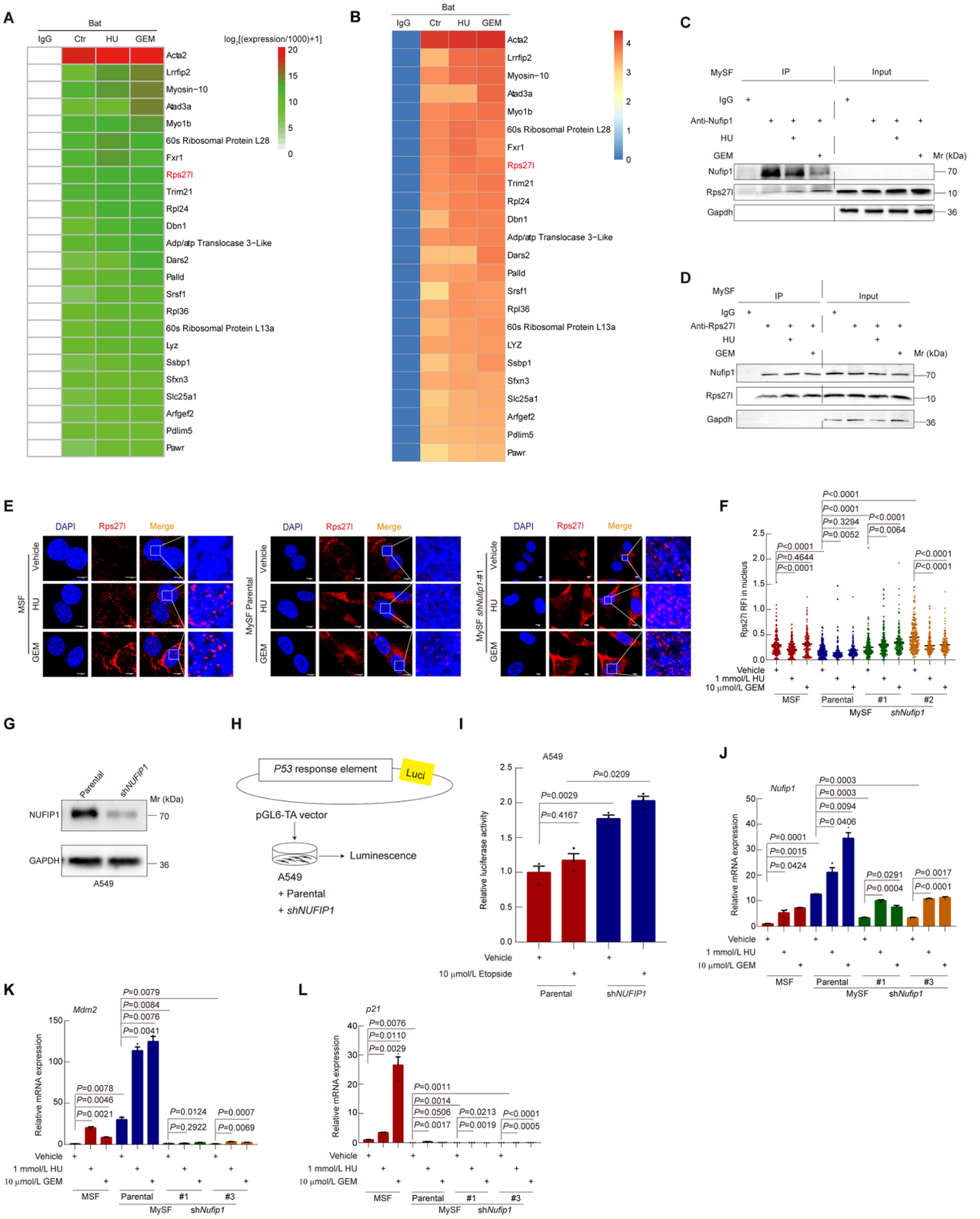

Figure 6 Proteomic interactome analysis reveals potential link between Nufip1 and Rps27l-Mdm2-P53 pathway

A, B: Heatmap of Nufip1-interacting proteins with increased binding under 1 mmol/L HU and 10 μmol/L GEM treatments using non-normalized (A) and normalized data (B). C, D: Immunoprecipitation combined with immunoblotting verification of Nufip1 interaction with Rps27l (C) and Rps27l interaction with Nufip1 (D) in MySF. Gapdh served as a negative control. E, F: Representative images (E) and statistical results (F) of relative fluorescence intensity of Rps27l in the nucleus of MySF with or without *Nufip1* knockdown, as well as in the nucleus of MSF. Scale bar: 5 μm. G: Validation of *NUFIP1* knockdown in A549 cells by immunoblotting. GAPDH served as a loading control. H: Schematic of P53 activity reporter system. I: Quantification of luciferase activity in A549 cells with or without etoposide-induced P53 induction. J–L: RT-qPCR detection of *Nufip1* (J), *Mdm2* (K), and *p21* (L) expression in MSF and MySF with or without *Nufip1* knockdown under 1 mmol/L HU or 10 μmol/L GEM treatment. Data represent mean±SEM. *n*=3 biologically independent experiments. *P*-values were calculated using a two-tailed *t*-test.

MySF at both the mRNA and protein levels, although its upstream transcriptional regulatory mechanisms remain poorly understood. It is also unclear whether *Nufip1* expression is universally elevated in other bat species or unique to *Myotis*, raising questions about the evolutionary conservation and lineage specificity of this regulatory mechanism. Second, the stronger protection of nascent DNA in bat cells compared to mouse cells is consistent with previous findings showing up-regulation of DNA replication and repair pathways in bats (Huang et al., 2016, 2019), as well as improved telomere protection (Li et al., 2023). Collectively, these findings suggest that bat cells may possess enhanced genomic stability pathways, including higher DNA repair efficiency, preferential selection of high-fidelity DNA repair pathways, and efficient chromosome stability during mitosis, each deserving of targeted functional validation. Third, although *Nufip1* clearly contributes to DNA replication stress resistance, it does not localize directly to replication forks. Indeed, a very recent study by Ming et al. (2025) reported that NUFIP1 mediates cross-talk between amino acid sensing and DNA damage response in intestinal inflammation, reinforcing the multifunctional nature of this protein in cellular stress adaptation. Given the unique ability of *Myotis* cells to protect nascent DNA, it is plausible that such cells may possess unique replication fork-associated proteins. Future studies employing nascent DNA-targeted proteomic techniques, such as isolation of proteins on nascent DNA (iPOND), may reveal novel fork-specific binding proteins in *Myotis* and uncover mechanisms that contribute to their extraordinary longevity (Tu et al., 2022).

DNA replication stress and the resulting genomic instability are considered major drivers of cellular senescence and organismal aging. In addition to performing classic protein translation functions, the ribosome biogenesis pathway plays an important role in cellular responses to external stressors, including senescence (Cheng et al., 2024; Nishimura et al., 2015), nucleolar stress regulation (Mende & Müller, 2021), and tumor initiation and progression (Orsolic et al., 2016; Pelletier et al., 2018; Truitt & Ruggero, 2016). These findings suggest a complex association between ribosome biogenesis and P53 signaling. Investigating this regulatory mechanism may provide strategies for effectively addressing cellular and organ aging driven by DNA replication stress response. The present study highlights the potential of *Myotis* cells as a new model for replication stress resistance and cell senescence research. Despite this promise, several technical challenges remain in the experimental development of bat cell systems, such as the isolation and culture of primary cells and incomplete genomic annotation. Moreover, our findings indicate that *Myotis* cells are particularly resistant to lentiviral infections, complicating routine gene knockdown and overexpression experiments. Optimization of delivery methods and the development of bat-specific genetic tools will be critical for unlocking the full potential of this model system. Interestingly, KEGG enrichment analysis revealed activation of the coronavirus disease pathway in *Myotis* cells under replication stress (Figure 5E, G). Indeed, many viruses, including coronaviruses, have been identified across bat species globally (Cui et al., 2019; Liang et al., 2021; Zhao et al., 2022, 2023). Despite this, no comprehensive studies have explored the interplay between ribosome biogenesis and the P53 signaling pathway in bats. The transcriptomic dataset generated in this study offers a valuable resource for future investigations into bat-specific mechanisms of stress adaptation and viral tolerance.

DATA AVAILABILITY

The RNA-seq data are available at the NCBI Gene Expression Omnibus (GEO) under BioProjectID PRJNA1252683, Genome Sequence Archive (GSA) at the National Genomics Data Center under accession No. PRJCA031395, and Science Data Bank (SDB) under DOI: 10.57760/sciencedb.23912. The datasets used and/or analyzed during the current study are available from the leading corresponding author (zhaobo@mail.kiz.ac.cn) upon reasonable request.

SUPPLEMENTARY DATA

Supplementary data to this article can be found online.

COMPETING INTERESTS

The authors declare that they have no competing interests.

AUTHORS' CONTRIBUTIONS

X.Y.H., X.Y.L., Y.L.Z., and X.W. carried out most of the experimental works and collected and analyzed the data. W.W. and G.J.L. conducted bioinformatic analysis. B.Z. and K.Q.L. designed and supervised the experiments. B.Z. and X.Y.H. wrote the manuscript. All authors read and approved the final version of the manuscript.

ACKNOWLEDGMENTS

We thank the staff members of the National Research Facility for Phenotypic & Genetic Analysis of Model Animals (Primate Facility) (https://cstr.cn/31137.02.NPRC) for providing technical support and assistance in data collection and analysis.

REFERENCES

Alshamrani AA, Bin Salman SB, Alsaleh NB, et al. 2024. miRNA-driven sensitization of breast cancer cells to doxorubicin treatment following exposure to low dose of zinc oxide nanoparticles. *Saudi Pharmaceutical Journal*, **32**(11): 102169.

Azpurua J, Ke ZH, Chen IX, et al. 2013. Naked mole-rat has increased translational fidelity compared with the mouse, as well as a unique 28S ribosomal RNA cleavage. *Proceedings of the National Academy of Sciences of the United States of America*, **110**(43): 17350–17355.

Caldecott KW. 2024. Causes and consequences of DNA single-strand breaks. *Trends in Biochemical Sciences*, **49**(1): 68–78.

Cheng YJ, Wang SW, Zhang H, et al. 2024. A non-canonical role for a small nucleolar RNA in ribosome biogenesis and senescence. *Cell*, **187**(17): 4770–4789. e23.

Cui J, Li F, Shi ZL. 2019. Origin and evolution of pathogenic coronaviruses. *Nature Reviews Microbiology*, **17**(3): 181–192.

Deisenroth C, Zhang Y. 2010. Ribosome biogenesis surveillance: probing the ribosomal protein-Mdm2-p53 pathway. *Oncogene*, **29**(30): 4253–4260.

Ercilla A, Feu S, Aranda S, et al. 2020. Acute hydroxyurea-induced replication blockade results in replisome components disengagement from nascent DNA without causing fork collapse. *Cellular and Molecular Life Sciences*, **77**(4): 735–749.

Franklin DA, Liu SJ, Jin AW, et al. 2023. Ribosomal protein RPL11 haploinsufficiency causes anemia in mice *via* activation of the RP-MDM2-p53 pathway. *Journal of Biological Chemistry*, **299**(1): 102739.

Gaillard H, García-Muse T, Aguilera A. 2015. Replication stress and cancer. *Nature Reviews Cancer*, **15**(5): 276–289.

Gorbunova V, Seluanov A, Kennedy BK. 2020. The world goes bats: living longer and tolerating viruses. *Cell Metabolism*, **32**(1): 31–43.

Gorbunova V, Seluanov A, Mao Z, et al. 2007. Changes in DNA repair during aging. *Nucleic Acids Research*, **35**(22): 7466–7474.

Healy K, Guillerme T, Finlay S, et al. 2014. Ecology and mode-of-life

explain lifespan variation in birds and mammals. *Proceedings of the Royal Society B: Biological Sciences*, **281**(1784): 20140298.

Heckenbach I, Mkrtchyan GV, Ezra MB, et al. 2022. Nuclear morphology is a deep learning biomarker of cellular senescence. *Nature Aging*, **2**(8): 742–755.

Hua R, Ma YS, Yang L, et al. 2024. Experimental evidence for cancer resistance in a bat species. *Nature Communications*, **15**(1): 1401.

Huang Z, Jebb DX, Teeling EC. 2016. Blood miRNomes and transcriptomes reveal novel longevity mechanisms in the long-lived bat, *Myotis myotis*. *BMC Genomics*, **17**(1): 906.

Huang ZX, Whelan CV, Foley NM, et al. 2019. Longitudinal comparative transcriptomics reveals unique mechanisms underlying extended healthspan in bats. *Nature Ecology & Evolution*, **3**(7): 1110–1120.

Huttlin EL, Bruckner RJ, Paulo JA, et al. 2017. Architecture of the human interactome defines protein communities and disease networks. *Nature*, **545**(7655): 505–509.

Jiang XY, Ma Y, Wang T, et al. 2023. Targeting UBE2T potentiates gemcitabine efficacy in pancreatic cancer by regulating pyrimidine metabolism and replication stress. *Gastroenterology*, **164**(7): 1232–1247.

Keane M, Semeiks J, Webb AE, et al. 2015. Insights into the evolution of Longevity from the Bowhead Whale Genome. *Cell Reports*, **10**(1): 112–122.

Kitao H, Iimori M, Kataoka Y, et al. 2018. DNA replication stress and cancer chemotherapy. *Cancer Science*, **109**(2): 264–271.

Levine AJ, Feng ZH, Mak TW, et al. 2006. Coordination and communication between the p53 and IGF-1–AKT–TOR signal transduction pathways. *Genes & Development*, **20**(3): 267–275.

Li KQ, Liu GJ, Liu XY, et al. 2023. EPAS1 prevents telomeric damage-induced senescence by enhancing transcription of *TRF1, TRF2*, and *RAD50*. *Zoological Research*, **44**(3): 636–649.

Li XK, Long JY, Yao CY, et al. 2024. The role of BTG2/PI3K/AKT pathway-mediated microglial activation in T-2 toxin-induced neurotoxicity. *Toxicology Letters*, **400**: 81–92.

Li YY, Lv QY, Zheng GT, et al. 2022. Unexpected expression of heat-activated transient receptor potential (TRP) channels in winter torpid bats and cold-activated TRP channels in summer active bats. *Zoological Research*, **43**(1): 52–63.

Liang J, Zhu CC, Zhang LB. 2021. Cospeciation of coronavirus and paramyxovirus with their bat hosts in the same geographical areas. *BMC Ecology and Evolution*, **21**(1): 148.

Liu X, Yang F, Li Y, et al. 2023. Evolution of p53 pathway-related genes provides insights into anticancer mechanisms of natural longevity in cetaceans. *Zoological Research*, **44**(5): 947–949.

Lubin E, Bryant L, Aicher J, et al. 2022. Analysis of histone variant constraint and tissue expression suggests five potential novel human disease genes: *H2AFY2, H2AFZ, H2AFY, H2AFV, H1F0*. *Human Genetics*, **141**(8): 1409–1421.

Makiuchi S, Tian Y, Fujimoto M, et al. 2024. DNA methylation alterations of *ADCY5, MICAL2*, and *PLEKHG2* during the developmental stage of cryptogenic hepatocellular carcinoma. *Hepatology Research*, **54**(3): 284–299.

McKeegan KS, Debieux CM, Boulon S, et al. 2007. A dynamic scaffold of pre-snoRNP factors facilitates human Box C/D snoRNP assembly. *Molecular and Cellular Biology*, **27**(19): 6782–6793.

Mende H, Müller S. 2021. Surveillance of nucleolar homeostasis and ribosome maturation by autophagy and the ubiquitin-proteasome system. *Matrix Biology*, **100–101**: 30–38.

Ming H, Tan J, Cao SY, et al. 2025. NUFIP1 integrates amino acid sensing and DNA damage response to maintain the intestinal homeostasis. *Nature Metabolism*, **7**(1): 120–136.

Nishimura K, Kumazawa T, Kuroda T, et al. 2015. Perturbation of ribosome biogenesis drives cells into senescence through 5S RNP-mediated p53 activation. *Cell Reports*, **10**(8): 1310–1323.

Ochman B, Limanówka P, Mielcarska S, et al. 2024. Associations of SEMA7A, SEMA4D, ADAMTS10, and ADAM8 with KRAS, NRAS, BRAF, PIK3CA, and AKT gene mutations, microsatellite instability status, and cytokine expression in colorectal cancer tissue. *Current Issues in Molecular Biology*, **46**(9): 10218–10248.

Orsolic I, Jurada D, Pullen N, et al. 2016. The relationship between the nucleolus and cancer: current evidence and emerging paradigms. *Seminars in Cancer Biology*, **37–38**: 36–50.

Pelletier J, Thomas G, Volarević S. 2018. Ribosome biogenesis in cancer: new players and therapeutic avenues. *Nature Reviews Cancer*, **18**(1): 51–63.

Quinet A, Carvajal-Maldonado D, Lemacon D, et al. 2017. DNA fiber analysis: mind the gap! *Methods in Enzymology*, **591**: 55–82.

Seim I, Fang XD, Xiong ZQ, et al. 2013. Genome analysis reveals insights into physiology and longevity of the Brandt's bat *Myotis brandtii*. *Nature Communications*, **4**(1): 2212.

Sikora E, Bielak-Zmijewska A, Mosieniak G. 2021. A common signature of cellular senescence; does it exist?. *Ageing Research Reviews*, **71**: 101458.

Tacutu R, Thornton D, Johnson E, et al. 2018. Human ageing genomic resources: new and updated databases. *Nucleic Acids Research*, **46**(D1): D1083–D1090.

Truitt ML, Ruggero D. 2016. New frontiers in translational control of the cancer genome. *Nature Reviews Cancer*, **16**(5): 288–304.

Tu Q, Liu XY, Yao XQ, et al. 2022. RETSAT associates with DDX39B to promote fork restarting and resistance to gemcitabine based chemotherapy in pancreatic ductal adenocarcinoma. *Journal of Experimental & Clinical Cancer Research*, **41**(1): 274.

Tyshkovskiy A, Ma SM, Shindyapina AV, et al. 2023. Distinct longevity mechanisms across and within species and their association with aging. *Cell*, **186**(13): 2929–2949. e20.

Wang HT, Xiao FH, Gao ZL, et al. 2024a. Methylation entropy landscape of Chinese long‐lived individuals reveals lower epigenetic noise related to human healthy aging. *Aging Cell*, **23**(7): e14163.

Wang L, Huang CZ, Lin WS, et al. 2024b. EIF3B affects the invasion and metastasis of hepatocellular carcinoma cells via the TGFBI/MAPK/ERK pathway. *Annals of Hepatology*, **30**(1): 101564.

Wang X, Jia JK, Wang Q, et al. 2024c. *Myotis* bat STING attenuates aging-related inflammation in female mice. *Zoological Research*, **45**(5): 961–971.

Wu ZM, Qu J, Liu GH. 2024. Roles of chromatin and genome instability in cellular senescence and their relevance to ageing and related diseases. *Nature Reviews Molecular Cell Biology*, **25**(12): 979–1000.

Xiong XF, Zhao YC, Tang F, et al. 2014. Ribosomal protein S27-like is a physiological regulator of p53 that suppresses genomic instability and tumorigenesis. *eLife*, **3**: e02236.

Zhang GJ, Cowled C, Shi ZL, et al. 2013. Comparative analysis of bat genomes provides insight into the evolution of flight and immunity. *Science*, **339**(6118): 456–460.

Zhao K, Zhang W, Li B, et al. 2022. Ecological study of cave nectar bats reveals low risk of direct transmission of bat viruses to humans. *Zoological Research*, **43**(4): 514–522.

Zhao L, Yuan JQ, Wang GQ, et al. 2024. Chromosome-level genome and population genomics of the intermediate horseshoe bat (*Rhinolophus affinis*) reveal the molecular basis of virus tolerance in *Rhinolophus* and echolocation call frequency variation. *Zoological Research*, **45**(5): 1147–1160.

Zhao RC, Niu S, Han P, et al. 2023. Cross-species recognition of bat coronavirus RsYN04 and cross-reaction of SARS-CoV-2 antibodies against the virus. *Zoological Research*, **44**(6): 1015–1025.